Accelerated and Motion-Robust In Vivo T_2 Mapping From Radially Undersampled Data Using Bloch-Simulation-Based Iterative Reconstruction

Noam Ben-Eliezer,* Daniel K. Sodickson, Timothy Shepherd, Graham C. Wiggins, and Kai Tobias Block

Purpose: Development of a quantitative transverse relaxation time (T_2)-mapping platform that operates at clinically feasible timescales by employing advanced image reconstruction of radially undersampled multi spin-echo (MSE) datasets.

Methods: Data was acquired on phantom and in vivo at 3 Tesla using MSE protocols employing radial k-space sampling trajectories. In order to overcome the nontrivial spin evolution associated with MSE protocols, a numerical signal model was precalculated based on Bloch simulations of the actual pulse-sequence scheme used in the acquisition process. This signal model was subsequently incorporated into an iterative model-based image reconstruction process, producing T_2 and proton-density maps.

Results: T_2 maps of phantom and in vivo brain were successfully constructed, closely matching values produced by a single spin-echo reference scan. High-resolution mapping was also performed for the spinal cord in vivo, differentiating the underlying gray/white matter morphology.

Conclusion: The presented MSE data-processing framework offers reliable mapping of T_2 relaxation values in a ~5-minute timescale, free of user- and scanner-dependent variations. The use of radial k-space sampling provides further advantages in the form of high immunity to irregular physiological motion, as well as enhanced spatial resolutions, owing to its inherent ability to perform alias-free limited field-of-view imaging. **Magn Reson Med 75:1346–1354, 2016. © 2015 Wiley Periodicals, Inc.**

Key words: quantitative MRI; T_2 mapping; model-based reconstruction; radial k-space sampling

INTRODUCTION

Quantitative mapping of the transverse relaxation time (T_2) in MRI can be used to detect pathological tissue changes in various clinical and research applications, including the diagnosis of brain ischemic stroke (1), assessment of cognitive impairment in multiple sclerosis (2), identification of cardiac edema and iron overload (3–5), cancer detection (6,7), and musculoskeletal imaging (8,9). Despite its potentially high impact, the estimation of T_2 values in vivo remains highly challenging due to the large number of spatial and temporal data points that need to be sampled in order to construct high-quality maps. The use of traditional single spin-echo (SE) imaging protocols is impractical for in vivo imaging due to their prolonged scan times (10s of minutes), which compromise patient throughput and lead to strong motion artifacts. A more realistic alternative is provided by multi-SE (MSE) protocols, which collect data at a series of distinct echo times (TE) during each repetition time (TR), thereby significantly shortening the overall scan time. An even higher efficiency can be achieved by sampling k-space radially, offering lower motion sensitivity (10)—and, as will be later seen—higher efficiency when scanning small structures due to its ability to acquire partial field of views (FOV), requiring smaller matrix sizes for a given target resolution. Its intrinsically incoherent undersampling artifacts can be further utilized for accelerating the acquisition either by employing compressed sensing (11,12) or using an inverse-problem formulation with analytical modeling of the acquired signal in the data reconstruction process (13). The advantages of radial MSE protocols, however, are offset by the complexity of reconstructing the desired image-space maps, particularly when dealing with undersampled data. Another major complication is the inherent bias of the MSE signal due to stimulated and indirect echoes, nonrectangular slice profiles, and radiofrequency transmit field (B_1^+) inhomogeneities. These cause the T_2 decay profile to deviate from the theoretical exponential model $S(t) = S_0\exp(-t/T_2)$, leading to significant T_2 estimation errors, which moreover vary between scanners and protocol versions due to practical differences between the corresponding pulse sequence implementation and experimental parameters.

A variety of approaches have been described for reconstructing undersampled radial MSE datasets. These are typically based on iterative processes that involve interpolation of the k-space data onto a Cartesian grid and fitting the temporal-domain data to a simplified model of the MSE T_2 decay curve (14–16). More advanced approaches exist such as the CUrve Reconstruction via pca-based Linearization with Indirect Echo compensation

(CURLIE) algorithm (17), which employs the slice-resolved, extended phase graph algorithm (18) to obtain more realistic decay curves for a model-based reconstruction of radially sampled datasets. The nonlinearity that is inherent to this type of reconstruction originates from the fact that the signal model incorporates the target maps via a nonlinear operation and is handled via principal component analysis-based linearization of the T_2 relaxation effect in MSE protocols. A recent report introduced the echo-modulation curve (EMC) T_2 mapping technique (19), which models the nonexponential T_2 decay curve through Bloch simulations tailored to the specific pulse sequence being employed rather than relying on the generic EPG model. This work presents first results of using the EMC algorithm in a model-based iterative reconstruction of radially sampled data. The generalized EMC-based signal model is designed to accurately reflect the pulse sequence scheme and parameter values, including the slice profile, radiofrequency (RF) pulse shapes, crusher gradients, and effect of spin relaxation during the RF pulses—a highly significant factor in light of the nonnegligible duration of the refocusing pulses with respect to the echo train length. The ensuing reconstruction procedure offers fast and reliable quantification of proton density (PD) and T_2 relaxation values in clinically feasible timescales. Validations are presented using phantoms and in vivo brain data, as well as high-resolution mapping of the gray/white matter in the spinal cord.

METHODS

Theoretical Formalism of Iterative EMC-Based Reconstruction

A detailed description of the principles underlying traditional iterative model-based reconstruction of radially sampled data can be found in (13). In essence, it is based on modeling the k-space signal using a forward acquisition operator given by

$$F_{t,c,j}(\rho, T_2) = \sum_{\overrightarrow{r} \in FOV} \rho(\overrightarrow{r}) \cdot e^{-t/T_2(\overrightarrow{r})} \cdot C_c(\overrightarrow{r}) \cdot e^{-i\overrightarrow{k}_j \cdot \overrightarrow{r}},$$

$$[1]$$

where t denotes the TE taking any discrete value determined by the sequence, j is an index into the set of consecutive signal-points acquired during each radial readout event $\overrightarrow{k}_j = [k_x, k_y]_j$, $\overrightarrow{r}$ denotes an image-space position $\overrightarrow{r} = [r_x, r_y]$, and C_c is the complex sensitivity profile of the cth coil. The resulting operator F represents a single readout event and reflects the sequential application of T_2 relaxation, coil sensitivity, and gradient-encoding operators on the proton density ρ. The unknowns being sought are the spatial distributions of T_2 and ρ, denoting the spin–spin relaxation and the spin density, respectively. Computation of the maps is performed using numerical minimization of a cost function, Φ, which evaluates the consistency of the T_2 and ρ parametric maps with respect to the raw k-space data

$$\Phi(\rho, T_2) = \frac{1}{2} \sum_t \sum_c \left\| \left(\overrightarrow{F}_{t,c} - \overrightarrow{y}_{t,c} \right) \right\|_2^2 = \Phi(\rho, T_2)$$
$$= \frac{1}{2} \sum_t \sum_c \sum_j \left(F_{t,c,j} - y_{t,c,j} \right)^2. \qquad [2]$$

The indices t and c run over the entire set of echo times and receive channels, whereas y represents the acquired k-space signal of a single readout event detected in channel c and at echo time t.

The relaxation model embedded in Eq. [1] reflects a purely exponential decay that breaks down for MSE pulse sequences on account of stimulated and indirect coherence pathways. These lead to significant errors, ranging up to as much as 50% to 100% of the true T_2 values when signal decay curves are fitted to a simple exponential (19). More accurate predictions can be obtained by using customized acquisition schemes (20,21) and tailored analytical signal models (22) or using algorithms that take into account the various factors that affect the spin dynamics in MSE sequences (18,23). In order to be compatible with the minimization of Eq. [2], any signal model furthermore needs to be well-defined and derivable throughout the parameter search space. Our implementation uses the numerical EMC algorithm described in reference [19], offering comprehensive modeling of MSE protocols based on computer simulations of the time-dependent Bloch equations for the actual MSE pulse sequence executed on the scanner. These simulations incorporate the exact RF pulse shapes, gradient waveforms, and other parameters to generate an estimated echo-modulation curve for a given pulse sequence scheme and set of experimental parameter values. Simulations are repeated for a range of T_2 and B_1^+ values, ultimately generating a database of EMCs, each associated with a unique $[B_1^+, T_2]$ value pair. The choice of considering the transmit field as an unknown in the fitting process stems from the relatively high variability of the B_1^+ field around the prescribed flip angle, a factor that is further accentuated due to the typically large number of refocusing RF pulses applied in MSE protocols. Various other parameters, such as the echo spacing, acquisition duration and bandwidth, and crusher gradient timings and moments, also affect the final decay curve. The value of these parameters can be accurately extracted from the vendor's pulse-program scheme and then used as an input to the simulation process. The role of T_1 relaxation has also been investigated in the context of the EMC algorithm; in agreement with previous reports (18,22,24), it was found to have very little effect on the experimental echo-modulation curve. It was therefore set to a fixed value of 0.5 sec for the phantom measurements and to 1 sec for the in vivo scans.

Updating Eq. [1] with an MSE-adapted relaxation term generated by the EMC algorithm yields

$$F_{t,c,j}(\rho, T_2) = \sum_{\overrightarrow{r} \in FOV} \rho(\overrightarrow{r}) \cdot EMC\left(B_1(\overrightarrow{r}), T_2(\overrightarrow{r}), t\right)$$
$$\cdot C_c(\overrightarrow{r}) \cdot e^{-i\overrightarrow{k}_j \cdot \overrightarrow{r}} \qquad [3]$$

A second step in integrating the EMC algorithm into the conjugate gradient (CG) iterative reconstruction is to define derivatives of the cost function Φ in Eq. [2] with respect to the values of the three unknowns (ρ, T_2, and B_1^+) at each spatial location. A derivative with respect to an arbitrary variable ξ will have the form (13)

$$\frac{\partial \Phi}{\partial \xi} = \frac{1}{2} \sum_t \sum_c \frac{\partial}{\partial \xi} \left[\sum_j \left(F_{t,c,j} - y_{t,c,j} \right) \overline{\left(F_{t,c,j} - y_{t,c,j} \right)} \right]$$

$$= \sum_t \sum_c \left[\Re \left\{ \sum_j \left(F_{t,c,j} - y_{t,c,j} \right) \frac{\partial}{\partial \xi} \overline{F_{t,c,j}} \right\} \right], \qquad [4]$$

where $\overline{(\cdot)}$ denoted the complex conjugate and $\Re\{\cdot\}$ is the real value. This reduces the problem to deriving F with respect to the ρ, T_2, and B_1^+ map values at each pixel. Plugging Eq. [3] into Eq. [4], we obtain

$$\frac{\partial \Phi}{\partial \rho_\upsilon} = \sum_t \sum_c EMC\left(B_{1,\upsilon}^+, T_{2,\upsilon}, t \right) \cdot$$

$$\underbrace{\Re \left\{ \overline{C_c(\overrightarrow{r}_\upsilon)} \cdot \sum_j \left(F_{t,c,j} - y_{t,c,j} \right) e^{+i \overrightarrow{k}_j \cdot \overrightarrow{r}_\upsilon} \right\}}_{\equiv Y} \qquad [5]$$

$$\frac{\partial \Phi}{\partial T_{2,\upsilon}} = \sum_t \sum_c \left[\frac{\partial EMC\left(B_{1,\upsilon}^+, T_{2,\upsilon}, t \right)}{\partial T_{2,\upsilon}} \right] \cdot \rho(\overrightarrow{r}_\upsilon) \cdot Y \qquad [6]$$

$$\frac{\partial \Phi}{\partial B_{1,\upsilon}^+} = \sum_t \sum_c \left[\frac{\partial EMC\left(B_{1,\upsilon}^+, T_{2,\upsilon}, t \right)}{\partial B_{1,\upsilon}^+} \right] \cdot \rho(\overrightarrow{r}_\upsilon) \cdot Y \qquad [7]$$

where υ is a voxel index running over the entire map's FOV, and Y is defined in Eq. [5].

The derivatives of the EMC term in Eqs. [6–7] were calculated numerically and are described in Appendix A. In practice, we found that the higher T_2-maps' accuracy is achieved by interpolating the numerical EMC database with respect to the discrete T_2 parameter. This is particularly valuable for data with short T_2 values for which a nonnegligible difference exists between echo-modulation curves of neighboring T_2 values. Using straightforward linear interpolation, the gap between each two simulated EMCs corresponding to neighboring T_2 values was populated with estimated EMCs to produce a higher level of discretization. A five-fold linear interpolation was used to increase the database discretization from $\Delta T_2 = 1$ ms to $\Delta T_2 = 0.2$ ms and was found to be sufficient for the postprocessing of all datasets.

Regularization

Notwithstanding the motion robustness entailed by radial sampling, phase inconsistencies, and partial voluming, effects can still result from irregular patient- or physiological-related motion—occurring, for example, in the prostate or spinal cord and translating into reconstruction noise. Several regularization strategies were investigated in this context, the most effective of which was the addition of Tikhonov regularization terms to the cost function, with separate λ_i-weighting for each of the fitted maps

$$\Phi(\rho, T_2) = \frac{1}{2} \left(\sum_t \sum_c \left\| \sum_j \left(F_{t,c,j} - y_{t,c,j} \right) \right\|_2^2 + \lambda_\rho \left\| \sum_{\overrightarrow{r} \in ROI} \rho(\overrightarrow{r}) \right\|_2^2 + \lambda_T \left\| \sum_{\overrightarrow{r} \in ROI} T_2(\overrightarrow{r}) \right\|_2^2 + \lambda_B \left\| \sum_{\overrightarrow{r} \in ROI} \tilde{B}_1^+(\overrightarrow{r}) \right\|_2^2 \right). \qquad [8]$$

The derivatives of the new terms are straightforward and simply proportional to the map values themselves. Apart from improving the reconstruction stability (25), the use of spatially specific regularization offered a convenient mechanism for imposing spatial smoothness on the B_1^+ map, which is expected to have slowly varying features. This was achieved by using a modified B_1^+ map (denoted by $\tilde{B}_1^+$) equal to the original map minus its mean value. The iterative process thus acts so as to minimize the B_1^+ variation around a certain baseline, better matching the physical system at hand. Further practical aspects pertaining to the regularization terms can be found in Appendix B.

Data Acquisition

Experiments were performed on a 3 T whole-body MR system (MAGNETOM Trio; Siemens AG Healthcare, Erlangen, Germany) for T_2 phantoms as well as human subjects. The experimental protocol involved running a radial MSE protocol (which constitutes the focus of this work) and two reference protocols: Cartesian MSE and Cartesian single-SE protocols. The radial protocol consisted of N_{EXC} spin excitations (one per TR) applying a 90° slice-selective RF pulse, followed by a train of echo-train length (ETL) SE readouts. Each of these readouts acquired a single spoke at a unique angular orientation. Refocusing pulses were enclosed by crusher gradients in

order to dephase spurious free-induction decay signals. The angular increment between each spoke (within an echo train as well as between consecutive echo trains) was fixed at the golden angle ($\sim$111.246°), generating a nonrepeating set of spoke angles. A key consideration in employing such a sampling scheme for mapping T_2 relaxation is the need to homogeneously cover the object's k-space separately for each of the echo times used. Because not every choice of [N_{EXC},ETL] values meets this condition, an allowed set of value pairs was determined via computer simulations of the k-space coverage per TE in the relevant parameter range. Reference T_2 values were generated from a Cartesian MSE protocol, sampling each k-space line multiple times following a 90° slice-selective excitation producing a series of two-dimensional (2D) images that correspond to increasing TEs. A second reference was collected where applicable (i.e., when scan times were not prohibitive) using a full single-SE protocol, which provided a more definitive map of the object's T_2 values.

Phantom scans were performed using a 12-element head coil array for data reception. Excitation was performed with the scanner's built-in body coil. The phantom is shown in Figure 1 and consists of a matrix of nine 15-ml plastic tubes containing purified water doped with manganese chloride ($MnCl_2$) concentrations of 0.070, 0.135, 0.270, 0.405, 0.540, 0.675, 0.800, 1.000, and 0.540 mM (corresponding to the tube numbers 1–9).
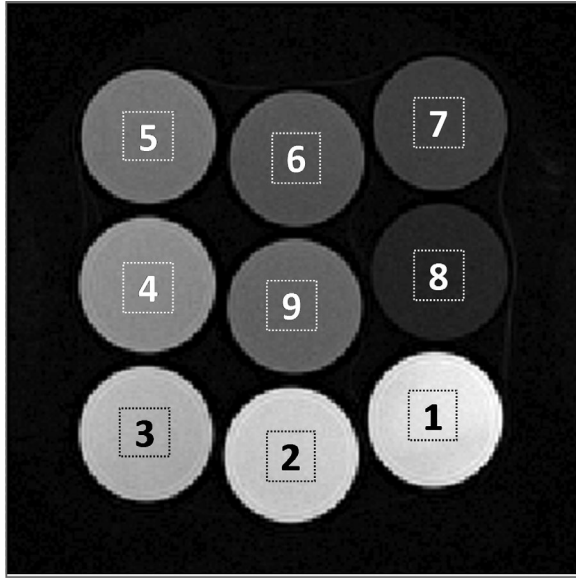
FIG. 1. T_2-weighted fast spin echo image of the nine-tube phantom used in this study. Tubes [1–8] were doped with varying concentrations of manganese chloride ($MnCl_2$), imparting to each tube a different T_2 relaxation time. Tubes #9 and #5 were prepared with similar concentrations in order to verify the T_2 mapping consistency over different spatial locations.

Tubes 5 and 9 were deliberately filled with identical concentrations in order to test spatial variation of the parameter extraction. This phantom offered a broad range of T_2 values with an average T_1/T_2 ratio of 13.8 ± 1.3, similar to human tissues (20,26). T_1 values were estimated using a double flip-angle, T_1-weighted, 3D-gradient echo protocol that was provided by the vendor. Phantom scans were repeated for refocusing angles $180°$, $150°$, $120°$, and $90°$ in order to assess the mapping stability over a range of commonly used values. Experimental parameters' values for all scans are summarized in Table 1. Similar scan times were chosen for the Cartesian and radial MSE protocols in order to be able—particularly in the in vivo scans—to compare the accuracy and efficiency of the two acquisition schemes under similar experimental conditions (see the Discussion section for more details).

In vivo validations were performed for the brain (N = 5) and cervical spinal cord (N = 5) of healthy volunteers under institutional guidelines and after obtaining written informed consent. Brain scans were performed with a receive-only 12-element head coil array, whereas the cervical spinal-cord scans were performed using a custom-built receive-only 8-element neck coil array. Parameters' values for all scans are delineated in Table 1. Single-SE data were not collected during the spinal cord scans due to severe artifacts caused by cerebrospinal fluid (CSF) pulsation as well as cardiac and respiratory motion. Partial alleviation of the physiologic motion associated with cardiac pulsation was achieved by triggering the acquisition using a pulse oximeter attached to the index finger of each volunteer with a 10-ms delay after the midsystolic time point (27). Acceleration was not applied in the Cartesian spinal cord scan due to the

Table 1
Summary of the Parameter Values for all Experiments Described in This Report

Parameter	Units	9-Tube Phantom			In Vivo Brain			In Vivo Spinal Cord	
		Single-SE Cartesian	Multi-SE Cartesian	Multi-SE Radial	Single-SE Cartesian	Multi-SE Cartesian	Multi-SE Radial	Multi-SE Cartesian	Multi-SE Radial
TR	(ms)	1,500	1,500	1,500	2,000	2,000	2,000	2,500	2,500
TE	(ms)	12,24,…,216	12,24,…,216	12,24,…,216	15,30,…,90	10,20,…,220	12,24,…,228	13,26,…260	13,26,…,143
ETL		1	18	18	1	22	19	20	11
N_{EXC}		–	–	98	–	–	95	–	124
Matrix size		192 × 192	192 × 192	–	128 × 108	192 × 162	–	–	–
Base resolution		192	192	192	128	192	192	128	240
FOV	(mm²)	110 × 110	110 × 110	110 × 110	220 × 185	220 × 185	220 × 220	96 × 96	96 × 96
Slice thickness*	(mm)	3	3	3	3	3	3	3	3
Refocusing angle	(deg)	90,120,150,180	90,120,150,180	90,120,150,180	180	180	180	180	180
BW_{acq}	(Hz/Px)	200	200	220	210	210	220	250	250
$N_{averages}$		1	1	2	1	1	1	1	1
Acceleration		None	None	3.1†	None	×2 GRAPPA	3.2†	None	3†
Total scan time	(h:mm:ss)	1:28:00	0:04:53	0:04:54	0:22:00	0:03:10	0:03:10	0:05:25	0:05:10

*Refocusing/excitation slice-thickness factor of 1.2 was used for all scans.

†Radial acceleration = [(base-res × π/2) × ETL] / [N_{exc} × ETL].

ETL, echo-train length; FOV, field of views; GRAPPA, generalized autocalibrating partially parallel acquisition; MSE, multi spin-echo; PD, proton density; SE, spin echo; TE, echo times; TR, repetition time.

Table 2
MnCl$_2$ Concentrations and Corresponding T$_2$ Values for the Phantom Shown in Figure 1

Tube No.	MnCl$_2$ (mM)	T$_1$(ms)	Cartesian Single-SE T$_2$Exponential Fit(ms)	Radial Sampling % Error in Multi-SE T$_2$EMC Fit				Cartesian Sampling % Error in Multi-SE T$_2$EMC Fit				% Error in Multi-SE T$_2$Exponential Fit			
α Refocus →		180°	180°	150°	120°	90°	180°	150°	120°	90°	180°	150°	120°	90°	
1	0.070	1424	116.7	5.3	0.5	1.4	4.9	0.9	1.1	3.9	5.9	35.6	42.2	59.4	99.3
2	0.135	877	68.5	2.5	6.0	7.3	8.6	3.6	3.8	5.5	9.1	33.7	39.4	53.4	85.1
3	0.270	528	36.9	1.7	7.9	7.9	11.1	1.6	2.7	4.9	7.9	40.1	46.1	68.6	110.0
4	0.405	363	23.5	2.2	7.7	6.8	11.5	0.0	0.4	3.0	6.4	45.1	54.5	74.0	132.8
5	0.540	235	17.9	1.8	5.0	0.6	1.1	0.0	1.7	3.9	11.7	53.1	79.3	97.2	182.1
6	0.675	214	14.4	2.2	9.7	6.9	12.5	1.4	0.0	2.1	8.3	56.3	74.3	88.9	172.2
7	0.800	155	11.9	8.6	10.1	9.2	4.2	0.8	0.8	6.7	11.8	67.2	82.4	106.7	213.4
8	1.000	120	9.7	7.8	7.2	6.2	10.3	4.1	8.2	13.4	8.2	71.1	51.5	112.4	230.9
9	0.540	287	17.8	2.3	9.0	8.4	12.9	1.1	1.1	2.2	6.2	52.2	71.9	83.1	143.3
		Mean % error:		3.8	7.0	6.1	8.6	1.5	2.2	5.1	8.4	50.5	60.2	82.6	152.1

T$_2$ values were obtained from either single-SE or MSE pulse sequence for four different refocusing flip-angles. Radial data was postprocessed using the EMC model-based reconstruction approach introduced in this report, whereas Cartesian data was postprocessed using either an exponential fit (for single-SE) or the EMC algorithm described in (19) (for MSE). Percent errors of MSE T$_2$ fits relative to single-SE T$_2$ fits (calculated as the absolute difference between the single-SE and MSE values, divided by the reference single-SE values) for various sampling and fitting methods are reported in columns 5–17. Average relative errors are listed in the bottom row. The third column states the T$_1$ values of each test tube, reflecting a relatively constant T$_1$/T$_2$ ratio of 13.8 ± 1.3.
EMC, echo-modulation curve; ETL, echo-train length; FOV, field of views; PD, proton density; SE = spin echo; T$_2$, transverse relaxation time; TE, echo times; TR, repetition time.

appearance of residual artifacts attributed to the generalized autocalibrating partially parallel acquisition reconstruction of such small regions of interest (ROIs).

Reconstruction

Postprocessing of the radial MSE data was performed using an in-house software package written in C/C++. As a preliminary step, the coil sensitivity profiles were estimated from the raw data according to procedure described in (28). T$_2$ and PD maps were generated by executing the nonlinear CG algorithm described in (29) and using the objective function in Eq. [8]. For the interpolation in k-space from a Cartesian grid to radial spokes and vice versa, a Kaiser-Bessel window with $L = 5$ and $\beta = 7.33$ was used, while utilizing the default two-fold oversampling factor of the raw data exported from the scanner (30). The stability and convergence of CG algorithms are typically sensitive to the relative scaling between the fitted parameters (13,16). This results from the intrinsically different baseline value of the PD, T$_2$, and B$_1^+$ maps. Improper scaling thus leads to disproportionate step sizes for the various parameters and may even cause divergence of the iterative process. Suitable tuning of the map values was achieved by scaling down the T$_2$ time axis by a factor of 250 and the B$_1^+$ map values by a factor of 2000. The optimal downscaling factor was found by examining the L$_2$-norm of the *gradient* of each map (Eqs. [5–7]) during the execution of the iterative process and setting the corresponding scaling factors in order to keep the relative gradients of the T$_2$ and B$_1^+$ maps in the range of 10% - 20% of the PD map gradient value. Tikhonov regularization of the PD and B$_1^+$ maps was incorporated into all data postprocessing by employing [$\lambda_\rho = 1$, $\lambda_T = 0$, $\lambda_B = 10$]. The CG process converged after 200 or more iterations for the phantom and brain

data, and at 150 … 200 iterations for the spinal cord data, after which noise-amplification artifacts emerged for low signal-to-noise (SNR) regions. As a last practical step, the CG-reconstruction process was restarted every N = 20 iterations for which the result of the nth run was used as an input for the nth + 1 run. Restarting the process allowed the previous search directions to become available because the CG-descent algorithm avoids repeating the same search directions in the parameter space more than once during each execution (31). This is a desired feature in light of the nonlinearity of the model being fitted, and it yielded faster and more reliable convergence.

T$_2$ maps were also generated from the single-SE and multi-SE Cartesian data. The single-SE data was processed by fitting each pixel in the corresponding time series of Digital Images and Communications in Medicine (DICOM) images to an exponential decay of the form $S(t) = S_0 \exp(-t/T_2)$. Although the resulting maps may be affected by residual diffusion bias, this effect is negligible in comparison to the variability of the T$_2$ values in vivo (32), and the maps were therefore used in this study as a baseline reference for the MSE maps. Cartesian MSE data was processed according to the EMC algorithm described in (19). In essence, the algorithm relies on matching the series of DICOM images to a precalculated database of simulated EMCs. This database is constructed numerically using Bloch-simulations of the pulse sequence scheme and incorporates the exact protocol's experimental parameter values, RF shapes, gradient waveforms, and event timing. Further information, including the source code of the simulations described in this report and the iterative model-based reconstruction code, as well as an EMC-based graphical-user-interface for reconstructing T$_2$ maps, is available online at (33). Computation time was approximately 1 minute for
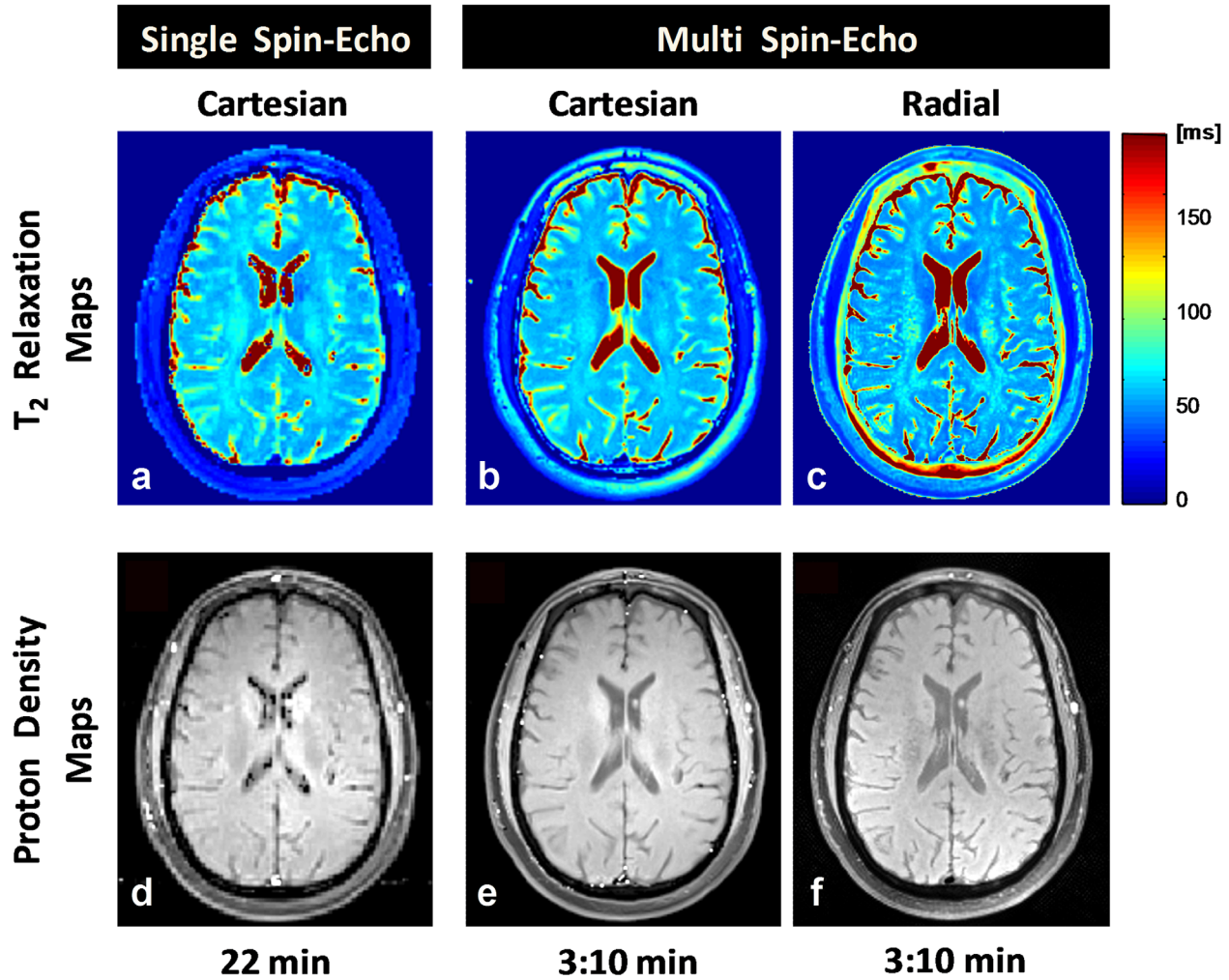
FIG. 2. In vivo T_2 and PD maps of a human brain in a healthy adult volunteer. (**a**) T_2 map derived from a single SE dataset and fitted to an exponential decay curve of the form $S(t) = S_0 \exp(-t/T_2)$. (**b**) T_2 map derived from a Cartesian multi-SE dataset via pixel-by-pixel matching of the experimental echo-modulation curve to the database of simulated EMCs as proposed in (19). (**d,e**) PD maps respectively matching the datasets in (a) and (b), derived by dividing the first echo-time image of each time series by the decay factor predicted by the corresponding T_2 maps. (**c,f**) T_2 and PD maps, derived from a radially sampled dataset acquired during the same scan session. These maps were generated jointly using the EMC model-based iterative reconstruction introduced in this report. EMC, echo-modulation curve; PD, proton density; SE = spin echo; T2, transverse relaxation time.

a matrix of 128×128 pixels using a standard desktop computer. This procedure resulted in assigning a unique T_2 value to each pixel, yielding the final T_2 map. As a second step, PD maps were calculated for both single-SE and MSE data by taking the T_2-weighted image of the first TE and extrapolating it to time $t = 0$ by dividing each pixel in the image by its T_2 decay factor $\exp(-TE/T_2)$ predicted by the T_2 map.

RESULTS

MnCl$_2$ Phantom Scans

Table 2 summarizes the measured T_2 values for the nine-tube phantom shown in Figure 1. Good correlation exists between the single-SE data and the radial MSE data (average P value < 1e–9). Fitting accuracy is furthermore relatively stable over the range of T_2 values and for refocusing flip angles down to 90°. Considering the single-SE values as the ground truth, slightly higher overall accuracy is

achieved by the Cartesian MSE T_2-mapping protocol for all refocusing flip angles assayed. This result is expected given the complexity of radial sampling and reconstruction compared to the Cartesian approach and the ideal conditions of scanning a phantom for which the improved motion robustness of radial trajectories is not manifested. A significant overestimation of the T_2 values emerges when using straightforward mono-exponential fit to process MSE data (rightmost four columns). This results from not accounting for stimulated and indirect echoes, which cause artificial elongation of the later parts of the echo train. The effect is further amplified when shifting from an optimal 180° refocusing flip angle because a higher percentage of the signal is then dominated by indirect echoes.

In Vivo Scans

Figure 2 compares representative T_2 and PD maps of the human brain produced from Cartesian single-SE, Cartesian
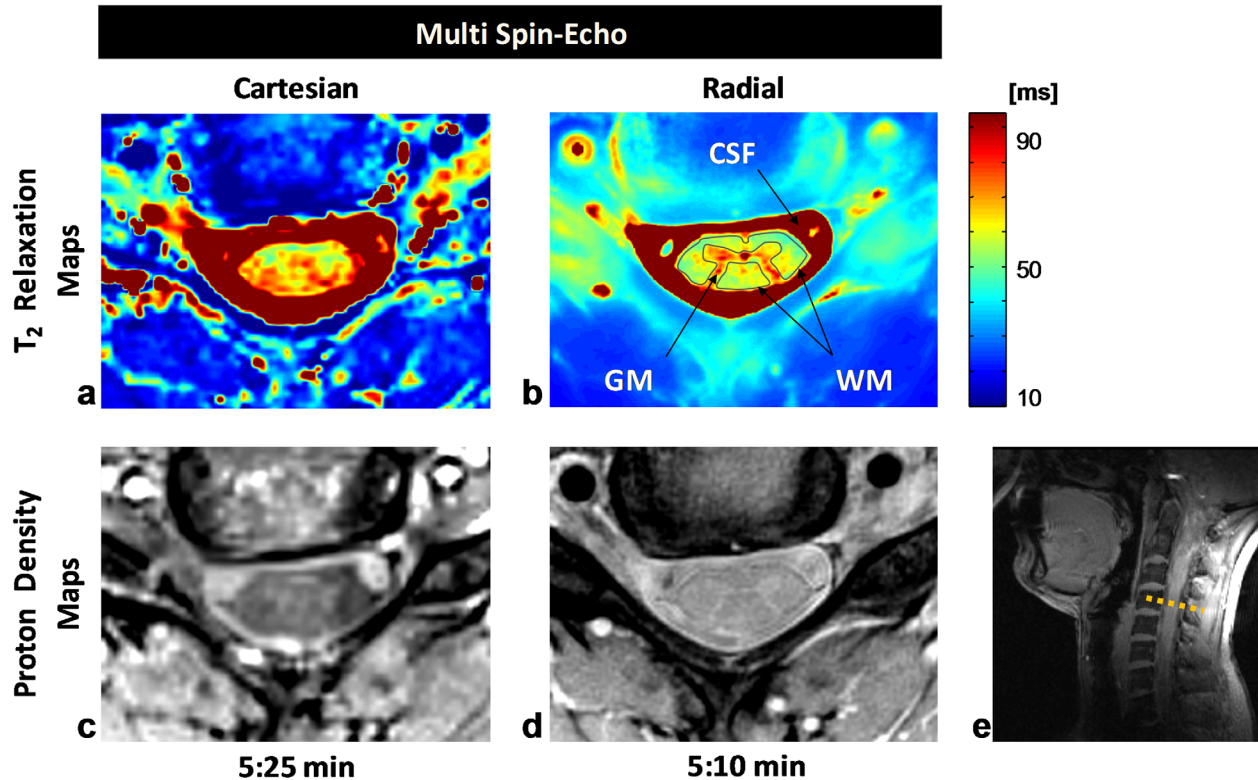
Multi Spin-Echo

FIG. 3. In vivo T_2 and PD maps for an axial slice in the cervical spinal cord of a healthy adult volunteer. (**a**) T_2 map derived from a Cartesian MSE dataset via pixel-by-pixel matching of the experimental echo-modulation curve to a database of simulated EMCs as proposed in (19). (**c**) PD map, matching the dataset in (a) derived by dividing the first echo-time image of the time-series by the decay factor predicted by the corresponding T_2 map. (**b,d**) T_2 and PD maps, derived from a radially sampled dataset collected during the same scan session and utilizing the nonfolding property of radial sampling to scan only half of the Cartesian FOVs, thereby increasing the acquisition efficiency. Maps were generated jointly using the EMC model-based iterative reconstruction described in this report. (**e**) Reference T_1-weighted sagittal image, marking the location of the axial slice in (a–d) (yellow dotted line). EMC, echo-modulation curve; MSE, multi spin-echo; PD, proton density; T2, transverse relaxation time.

MSE, and radial MSE data. Very good correlation is observed between all three data sets, with the MSE protocols providing higher spatial resolutions owing to the extensive scan times that would have been required in order to achieve a similar resolution using a single-SE protocol. CSF pulsation occurring over the 22-minute scan still affects the single-SE maps and manifests as residual artifacts within the ventricles. Apart from the excellent match to the reference Cartesian data, the radially sampled maps also offer slightly higher definition and better coverage of the peripheral scalp area, a result that can be ascribed to its higher robustness to physiological motion.

The potential advantages of radial sampling are further illustrated in Figure 3, showing T_2 and PD maps of an axial slice at the C3 vertebrae of the cervical spinal cord (slice location shown in panel 3e). The small features of this anatomy pose a considerable challenge for T_2 mapping, which is moreover exacerbated by in-plane CSF pulsations and through-plane flow. Panels 3b,d demonstrate the ability of radial sampling to alleviate these motion-related artifacts and extract high-resolution anatomical information, clearly differentiating the gray and white matter tracts within the spinal cord. Slight blurring appears in the peripheral parts of these maps as a result of excluding these regions from the spatial-domain regularization terms in (8) in order to achieve faster convergence

at the ROI (see Methods section). A corresponding set of Cartesian sampled maps, acquired during the same scan session and using identical parameters, are shown in panels 3a,c. Although the Cartesian PD map exhibits the same general morphology as the radial map, this data is strongly affected by motion and fails to produce consistent T_2 maps or extract the internal features of the cord. Quantitative measurements on the segmented ROIs in panel 3b produced mean T_2 values equal to 58.9 ± 4.0 ms for white matter and 71.4 ± 12.6 ms for gray matter. Although the lack of gold standard measurements for the spinal cord prevents conclusive validation of these values, a close match exists between the gray matter T_2 value and previously reported value of 73 ± 3 ms (27). Further corroborations are provided by the T_2 values of the surrounding muscle tissue (31.8 ± 0.3 ms), which match values reported in the literature (34,35), and by the good correspondence of the gray/white matter T_2 ratio ($\sim$1.2) to similar values reported for brain tissues (36,37).

DISCUSSION

The EMC algorithm offers fast and accurate mapping of tissue T_2 and PD values, independent of the specific scanner type and pulse sequence implementation. Its combination with radial sampling offers improved immunity to

physiological and patient motion and, owing to the inherent multidimensional readout-oversampling of this acquisition scheme, allows scanning partial FOVs at arbitrary spatial resolutions, thereby further shortening scan times. Although this report does not fully explore the acceleration potential afforded by radial sampling, the use of MSE-based protocols with acquisition times that are comparable to two-fold accelerated Cartesian MSE protocols already yielded clinically feasible scan times, and more importantly made it possible to highlight the advantages of radial sampling given similar scan conditions.

Notwithstanding the good correlation between the T$_2$ maps produced by the EMC model-based reconstruction and the reference Cartesian values, this type of reconstruction is still challenging to optimize. This is mostly reflected in the sensitivity of the iterative procedure to the relative scaling between the fitted variables, affecting both convergence accuracy and speed (17). In practice, we found the relative scaling to have lower significance when processing the phantom and brain T$_2$ maps, while having higher effect on the spinal cord data. This is not unexpected because the latter data is of *a priori* lower quality, and as such it requires more careful tuning of the iterative reconstruction in order to accentuate signal changes pertaining to the encoded MR parameters as opposed to spurious motion-related perturbations and noise. Akin to the influence of regularization, a tradeoff was observed when choosing a suitable scaling value for which excessive downscaling caused blurring, whereas insufficient downscaling failed to effectively remove noise. In practice, stable convergence was reached by identifying a "sweet-spot" for each scaling-parameter value having a typical tolerance of $\pm 20\%$ for the B$_1$ scaling and $\pm 10\%$ for the T$_2$ scaling. These values were found empirically and employed in the postprocessing of all acquired datasets.

The high quality of the radially sampled in vivo maps attests to the value of this sampling scheme, particularly in the spinal cord region. These maps are, to the best of our knowledge, the first successful attempt at differentiating the T$_2$ values of the white- and gray-matter structures within the spinal cord. In this case, the submillimeter spatial resolution requirements for mapping these structures are only met owing to the efficiency and motion robustness of radial sampling. Although it is difficult to estimate the motion-related blurring that occurs during in vivo scans (and therefore to state with confidence whether the prescribed resolution is actually reflected in the final maps), it is evident that the ensuing spatial definition is superior to what can be realized using Cartesian sampling, clearly illustrating the advantages of radial sampling in the face of irregular physiological motion. Further information regarding the influence of motion on radial sampling can be found in (10,38). Investigation of its effect on the T$_2$ mapping accuracy is under way and will be reported in future publications.

Extending the iterative EMC model-based reconstruction to support other contrasts is feasible and the subject of ongoing work. A general requirement for accurate mapping is that the target MR parameters are sufficiently encoded during the signal acquisition process. This can include the use of short TRs for increased T$_1$ weighting, implementation of variable refocusing flip-angles for improved B$_1^+$ encoding, or optimization of the echo spacing in order to sample both short and long TEs in order to effectively encode multiple T$_2$ components. A generalized reconstruction framework can then be utilized to estimate multiple parameters jointly from a single acquisition in a manner analogous to that used in the recently proposed MR fingerprinting technique (12). In contrast to MR fingerprinting, which relies on incoherent aliasing artifacts in order to handle highly undersampled data, the EMC model-based approach incorporates information about the sampling trajectory directly into the signal model and tries to remove, rather than circumvent, the aliasing related artifacts. It can therefore handle both incoherent and coherent aliasing patterns and support arbitrary k-space geometries. It should be noted that the EMC database computation time is expected to increase with each additionally encoded parameter. These calculations, however, are highly parallelizable and thus are well suited for acceleration using multicore processing units such as graphical processing units.

CONCLUSION

This work demonstrates the feasibility of using radial sampling for rapid and robust mapping of T$_2$ relaxation in vivo. The combination of the EMC algorithm with model-based iterative reconstruction allows accurate extraction of the tissue T$_2$ values while removing the protocol- and parameter-dependent variability that impairs conventional exponential fitting. The ensuing acquisition and postprocessing framework can be used for quantitative diagnosis of pathologies that require investigation of high-resolution structures embedded within larger tissue regions (e.g., the internal nuclei of the thalamus for direct targeting in functional neurosurgery) and of body regions affected by irregular physiological motion, such as the spinal cord and prostate.

ACKNOWLEDGMENT

APPENDIX A

The derivatives of the echo-modulation curve (EMC) term in Eqs. [6–7] can be calculated numerically using the formal definition $df/dx = [f(x + h) - f(x)]/h$. Since the EMC function is defined at discrete transverse relaxation time (T$_2$) values, its derivative with respect to an arbitrary value $T_{2,v}$ can be computed as the weighted average of the derivative above and below this value,

$$\frac{\partial EMC}{\partial T_{2,v}} \equiv \frac{1}{2} \left[\frac{EMC\left(T_{2,v}^{\text{up}}\right) - EMC(T_{2,v})}{T_{2,v}^{\text{up}} - T_{2,v}} + \frac{EMC(T_{2,v}) - EMC\left(T_{2,v}^{\text{down}}\right)}{T_{2,v} - T_{2,v}^{\text{down}}} \right]$$

[A1]

where $T_{2,v}^{\text{up}}$ and $T_{2,v}^{\text{down}}$ represent the neighboring EMC simulation points. An identical formalism can be then

applied for the calculation of the derivative with respect to B_1, υ^+ in Eq. [7].

APPENDIX B

Another practical aspect, attributed to the use of spatially specific regularization terms, was the ability to exclude low signal-to-noise (SNR) regions from the reconstruction process, thereby focusing the reconstruction on targeted regions-of-interest and promoting faster convergence. To that end, an initial transverse relaxation time (T_2)-weighted estimate of the anatomy was generated via straightforward gridding of the entire dataset onto a Cartesian k-space grid, followed by Fourier transformation to the image domain. This image was normalized and then used to create a binary mask in which all regions with signal below a predefined threshold $\delta_{mask} = 0.1$ were set to zero. The resulting mask was finally applied in the Tikhonov terms of the cost function in Eq. [8] to exclude low SNR regions.

REFERENCES

1. Siemonsen S, Mouridsen K, Holst B, Ries T, Finsterbusch J, Thomalla G, Ostergaard L, Fiehler J. Quantitative T2 values predict time from symptom onset in acute stroke patients. Stroke 2009;40:1612–1616.
2. Lund H, Jønsson A, Andersen J, Rostrup E, Paulson O, Sørensen P. Cognitive deficits in multiple sclerosis: correlations with T2 changes in normal appearing brain tissue. Acta Neurol Scand 2012;125:338–344.
3. Cury R, Shash K, Nagurney J, et al. Cardiac magnetic resonance with T2-weighted imaging improves detection of patients with acute coronary syndrome in the emergency department. Circulation 2008;118:837–844.
4. Eitel I, Friedrich M. T2-weighted cardiovascular magnetic resonance in acute cardiac disease. J Cardiovasc Magn Reson 2011;13:13.
5. Ptaszek L, Price E, Hu M, Yang P. Early diagnosis of hemochromatosis-related cardiomyopathy with magnetic resonance imaging. J Cardiovasc Magn Reson 2005;7:689–692.
6. Liu W, Turkbey B, Sénégas J, Remmele S, Xu S, Kruecker J, Bernardo M, Wood B, Pinto P, Choyke P. Accelerated T2 mapping for characterization of prostate cancer. Magn Reson Med 2011;65:1400–1406.
7. Farraher S, Jara H, Chang K, Ozonoff A, Soto JA. Differentiation of hepatocellular carcinoma and hepatic metastasis from cysts and hemangiomas with calculated T2 relaxation times and the T1/T2 relaxation times ratio. J Magn Reson Imaging 2006;24:1333–1341.
8. Pan J, Pialat J, Joseph T, Kuo D, Joseph G, Nevitt M, Link T. Knee cartilage T2 characteristics and evolution in relation to morphologic abnormalities detected at 3-T MR imaging: a longitudinal study of the normal control cohort from the Osteoarthritis Initiative. Radiology 2011;261:507–515.
9. Patten C, Meyer R, Fleckenstein J. T2 mapping of muscle. Semin Musculoskelet Radiol 2003;7:297–305.
10. Glover G, Pauly J. Projection reconstruction techniques for reduction of motion effects in MRI. Magn Recon Med 1992;28:275–289.
11. Doneva M, Börnert P, Eggers H, Stehning C, Sénégas J, Mertins A. Compressed sensing reconstruction for magnetic resonance parameter mapping. Magn Res Med 2010;64:1114–1120.
12. Ma D, Gulani V, Seiberlich N, Liu K, Sunshine J, Duerk J, Griswold M. Magnetic resonance fingerprinting. Nature 2013;14:187–192.
13. Block K, Uecker M, Frahm J. Model-based iterative reconstruction for radial fast spin-echo MRI. IEEE Trans Med Imaging 2009;28:1759–1769.
14. Altbach M, Outwater E, Trouard T, Krupinski E, Theilmann R, Stopeck A, Kono M, Gmitro A. Radial fast spin-echo method for T2-weighted imaging and T2 mapping of the liver. J Magn Reson Imag 2002;16:179–189.
15. Altbach M, Bilgin A, Li Z, Clarkson E, Trouard T, Gmitro A. Processing of radial fast spin-echo data for obtaining T2 estimates from a single k-space data set. Magn Res Med 2005;54:549–559.
16. Huang C, Graff C, Clarkson E, Bilgin A, Altbach M. T2 mapping from highly undersampled data by reconstruction of principal component coefficient maps using compressed sensing. Magn Reson Med 2012;67:1355–1366.
17. Huang C, Bilgin A, Barr T, Altbach M. T2 relaxometry with indirect echo compensation from highly undersampled data. Magn Reson Med 2013;70:1026–1037.
18. Lebel R, Wilman A. Transverse relaxometry with stimulated echo compensation. Magn Reson Med 2010;64:1005–1014.
19. Ben-Eliezer, N, Sodickon, DK, and Block, KT. Rapid and accurate T2 mapping from multi-spin-echo data using Bloch-simulation-based reconstruction. Magn Reson Med 2015;73:809–817.
20. McKenzie C, Chen Z, Drost D, Prato F. Fast acquisition of quantitative T2 maps. Magn Reson Med 1999;41:208–212.
21. Anderson S, Sakai O, Soto J, Jara H. Improved T2 mapping accuracy with dual-echo turbo spin echo: effect of phase encoding profile orders. Magn Reson Med 2013;69:137–143.
22. Zur Y. An algorithm to calculate the NMR signal of a multi spin-echo sequence with relaxation and spin-diffusion. J Magn Reson 2004;171:97–106.
23. Petrova M, Doktorov A, Lukzen N. CPMG echo amplitudes with arbitrary refocusing angle: explicit expressions, asymptotic behavior, approximations. J Magn Reson 2011;212:330–343.
24. Prasloski T, Mädler B, Xiang Q, MacKay A, Jones C. Applications of stimulated echo correction to multicomponent T2 analysis. Magn Reson Med 2012;67:1803–1814.
25. Fernandez-Martineza, JL, Pallerob, JLG, Fernandez-Muniza, Z, and Pedruelo-Gonzaleza, LM. The effect of noise and Tikhonov's regularization in inverse problems. Part II: the nonlinear case. J Appl Geophys 2014. doi: 10.1016/j.jappgeo.2014.05.005.
26. Kim D, Jensen J, Wu E, Sheth S, Brittenham G. Breathhold multiecho fast spin-echo pulse sequence for accurate R2 measurement in the heart and liver. Magn Reson Med 2009;62:300–306.
27. Smith S, Edden R, Farrell J, Barker P, Van Zijl P. Measurement of T1 and T2 in the cervical spinal cord at 3 tesla. Magn Reson Med 2008;60:213–219.
28. Block K, Uecker M, Frahm J. Undersampled radial MRI with multiple coils. Iterative image reconstruction using a total variation constraint. Magn Reson Med 2007;57:1086–1098.
29. Hager W, Zhang H. A new conjugate gradient method with guaranteed descent and an efficient line search. Siam J Optim 2005;16:170–192.
30. Beatty P, Nishimura D, Pauly J. Rapid gridding reconstruction with a minimal oversampling ratio. IEEE Trans Med Imaging 2005;24:799–808.
31. Nocedal G, Wright S. Conjugate Gradient Methods, in Numerical Optimization. New York, NY: Springer-Verlag, 1999.
32. Stanisz G, Odrobina E, Pun J, Escaravage M, Graham S, Bronskill M, Henkelman RM. T1, T2 relaxation and magnetization transfer in tissue at 3T. Magn Res Med 2005;54:507–512.
33. .EMC based T2 mapping software package. Available at: http://cai2r.net/resources/software/emc-based-t2-mapping-package.
34. Gold G, Han E, Stainsby J, Wright G, Brittain J, Beaulieu C. Musculoskeletal MRI at 3.0 T: relaxation times and image contrast. AJR Am J Roentgenol 2004;183:343–351.
35. Jordan C, Saranathan M, Bangerter N, Hargreaves B, Gold G. Musculoskeletal MRI at 3.0 T and 7.0 T: a comparison of relaxation times and image contrast. Eur J Radiol 2013;82:734–739.
36. Jezzard P, Duewell S, Balaban R. MR relaxation times in human brain: measurement at 4 T. Radiology 1996;199:773–779.
37. Bieri O, Scheffler K, Welsch G, Trattnig S, Mamisch T, Ganter C. Quantitative mapping of T2 using partial spoiling. Magn Reson Med 2011;66:410–418.
38. Chandarana H, Block K, Rosenkrantz A, Lim R, Kim D, Mossa D, Babb J, Kiefer B, Lee V. Free-breathing radial 3D fat-suppressed T1-weighted gradient echo sequence: a viable alternative for contrast-enhanced liver imaging in patients unable to suspend respiration. Invest Radiol 2011;46:648–653.